Modelling the Influence of Microstructural Morphology and Triple Junctions on Hydrogen Transport in Nanopolycrystalline Nickel

*Sathiskumar Jothi, T.N.Croft, S. G. R. Brown,

College of Engineering, Swansea University, Singleton Park, Swansea SA2 8PP, UK

*S.Jothi@swansea.ac.uk; *jsathiskumar@gmail.com

Hydrogen transport in nanopolycrystalline (NPC) face centred cubic (FCC) nickel has received considerable attention as a result of the material's unique structural embrittlement behaviour. Triple junctions, where three grain boundaries meet, play an important role in hydrogen diffusion. Experiments have indicated that hydrogen transport at a triple junction (TJ) is orders of magnitude greater. In this contribution, a multiphase NPC model is proposed and used to investigate the influence on hydrogen transport of TJs within the surface of the NPC nickel using finite nanostructural element analyses. This 2D multiphase NPC model increases the density of triple junctions as the grain size reduces. The multiphase NPC model consists of two phases comprising nano grain interiors (GI) and intergranular phases. The intergranular (Ig) phase is divided into grain boundary affected zones (GBAZ) regions and TJ regions. The results of this finite nanostructural analysis show that hydrogen transport is enhanced at TJs and the bulk diffusion of hydrogen in NPC material is faster as the volume fraction of TJ increases and nano grain size decreases. The accumulation of hydrogen in three phase (GI, GBAZ, and TJ) microstructures is higher than the two phase (GI and Ig) microstructure case. The accumulation of hydrogen in TJ and Ig are heterogeneous in NPC nickel. The importance of the microstructural morphology in terms of the presence of pores, fine grains in TJ, changes in the shape of TJ with changes in the density of TJ and a TJ effect related to hydrogen transport in NPC nickel is all evidenced. This means that the TJ and microstructural morphology cannot be neglected when predicting hydrogen transport in a NPC nickel.

Keywords: Nano-structures; Interface/interphase; Microstructures; Computational modelling; Triple Junction.

1. Introduction:

Many researchers, scientists and industrialists are working towards a greater understanding of microstructural TJs in NPC material because of the change in properties of this material with changing microstructural nano grain sizes [1-12, 14-31, 33-37, and 40-44]. The expected significant change in the properties of the NPC materials, when decreasing the

grain size of NPC material, is partially explained by the increase in the density of TJs [1-3, 17]. The microstructural morphology such as grain size, interfacial grain boundary (GB), pores in TJs, fine grains in TJs and Triple Junction (TJ) shapes, width and size may also affect the physical properties, atomic transport and properties in NPC materials [7-12, 14-16, 31-34, 42]. The microstructural TJ diffusivity in NPC materials is higher than the diffusivity at microstructural interfacial GBs due to the structurally weaker bonding nature of TJs [17-21, 35-36]. Rapid TJ diffusion has important consequences for a range of properties of NPC materials such as the hydrogen transport, super elasticity and diffusional creep [1-3, 22-25, 32]. Electrodeposited NPC nickel has several engineering and aerospace industrial applications; one such application in aerospace industries is in the thrust chambers of rocket engines. Typical applications have been in the Ariane satellite launcher and the main engine of the NASA Space Shuttle as shown in Figure 1 (a) [1,38]. Production of NPC material using electrodeposition pulse plating processing techniques have been subjected to extensive research in recent years due to the economic viability of the process [37,39]. During the manufacturing process of NPC nickel hydrogen impurities are introduced into the material. The presence of hydrogen atoms in steel and nickel increases the potential for embrittlement related failures [45-47]. Consequently electrodeposited NPC nickels have gained the attention of the scientific community.

The diffusivity properties of hydrogen atom transport in electrodeposited NPC nickel are different in the grain interior (GI), the grain boundary (GB), the grain boundary affected zone (GBAZ) and the triple junction (TJ) [2]. The intergranular (Ig) region is composed of GBAZ and TJ. A high density of TJs is found in such materials due to their small grain size. To control the hydrogen embrittlement of electrodeposited NPC nickel it is important to consider the properties and microstructural characteristic of the TJ. The hydrogen diffusivity in the TJ is approximately three times the diffusivity in GBs which in turn is approximately seventy times the diffusivity in the GI [2]. Locations where the concentration of hydrogen atoms is higher in this material will have an increased tendency for the initiation of embrittlement related failure. The TJ, where three grain boundaries meet, plays an important and dominant role in NPC electrodeposited nickel with respect to hydrogen transport due to the higher relative volume fraction, weaker bonding structures and higher diffusivity compared to the GB and the GI [3]. The presence of residual pores, cluster vacancies and very fine grains in NPC nickel are reported previously [3, 4, and 5]. It shows that the NPC nickels are different from conventional coarse grain nickel materials. Thus it is important to treat the TJ as an independent defect and consider its microstructural morphology to

investigate the hydrogen transport in electrodeposited NPC nickel both in computational and experimental studies. Figure 2 (a), (b) and (c) shows the 2D EBSD (Electron backscattered diffraction) experimental microstructural image of NPC Nickel with decrease in average grain sizes respectively. The decrease in average grain size corresponds to an increase in number of triple junctions. Figure 2 (d), (e) and (f) shows a schematic view of the multiphase NPC model and the increase in the number of triple junctions as the grain size reduces. The structure of TJs depends on the random arrangement and orientation of neighbouring adjacent crystal grains [6]. Grain size effects play a vital role in determining the diffusivity of hydrogen in these materials. Decreasing the grain size will increase the volume fraction of TJs [2, 3].

In the first part of this paper, a mechanism is proposed for the effects of triple junctions on the diffusion of hydrogen with respect to grain size. The proposed finite element (FE) model accounts for the effect of triple junctions by increasing the average density of TJs as the average grain size of the NPC material decreases in the range 50nm - 5nm. The result of the analysis shows that the effective diffusion in NPC material increases with the increase in the relative volume fraction of the TJs. The influence of the shape of TJs (i.e. sharp corner shaped TJs and round corner shaped TJs) is also investigated with respect to hydrogen transport.

In the second part of this paper, four different mesoscale NPC models with different synthetic microstructures are investigated. The first mesoscale microstructure model contains a single crystal. The second mesoscale NPC microstructure model contains normal nano grains (NNG), GBAZ and TJ. These two models are adopted in this study to i) investigate the delay mechanism of hydrogen transport in a single crystal microstructure when compared to NPC microstructures with NNG, GBAZ and TJs and ii) to investigate the faster mechanism of hydrogen transport in NPC mesoscale microstructures in the presence of NNG, GBAZ and TJs. The faster mechanism of hydrogen is due to the presence of a higher density of TJs in NPC material. The third mesoscale microstructure model contains NNG, GBAZ and pores in the TJs. The fourth mesoscale microstructure model contains NNG, GBAZ and fine nano grains (FNGs) in TJs. The third and fourth mesoscale models are used to investigate the hydrogen transport mechanisms in NPC nickel microstructural TJs containing pores or FNGs. The effects of the TJs, pores and FNGs on the hydrogen transport behaviours of NPC materials are numerically analysed.

2. Computational Experimental Procedure:

2.1. ***Mesoscale microstructure model for NPC material***:

In this section a mesoscale model is developed to enable simulation of NPC materials with various synthetic microstructures. The basic synthetic microstructure model is based on the model proposed by Meyers and Ashworth (MA) [7] which contains two phases i.e. grain and grain boundaries in the NPC material, a more detailed description about this model can be found elsewhere [7-12]. The MA model is the base model which is here extended to study the effect of TJs on hydrogen transport in NPC material by including TJs as a third phase in the model. So, in this work the MA concept is extended to a three phase synthetic microstructural model as shown in Figure 3 to study the effect of TJs on hydrogen transport in NPC nickel. Various synthetic microstructures are generated computationally for NPC materials for combinations of three different average grain sizes, three different TJ densities, two different TJ shapes, nano pores in the TJ, fine nano grains in TJ and a single crystal case. These 2 dimensional synthetic microstructural geometries are generated in heterogeneous form with polycrystalline aggregates composed of two phases, GI phase and Ig phase. The Ig phase is further divided into two regions to form three phase regions GI, GBAZ and TJ using modified Voronoi tessellation theory. The geometric specification algorithm is developed and coded using MATLAB [49] and the Python programming language and then these codes are embedded into an ABAQUS FE code [13] to develop the heterogeneous mesoscale microstructural models of NPC material. Detailed information about the computationally developed synthetic mesoscale microstructure using modified Voronoi tessellation technique can be found elsewhere [8, 10, and 48].

2.2 FE Model development:

The computational experimental technique used to simulate hydrogen transportation was developed using the FE method and analysed using commercial FE analysis software ABAQUS. The test cases for the prediction of hydrogen transport in NPC material consists of a rectangular specimen through which the concentration of hydrogen diffuses in one direction, from the left side of the domain to right side of the domain in the *x* direction. Zero initial hydrogen is present in the specimen. For boundary conditions a higher concentration of hydrogen (0.0001ppm) is present on the left hand side of the specimen with zero flux on the right hand side of the specimen and a constant temperature of 25 °C applied. These conditions are assumed in the absence of trapping and other phenomena. There is no transport of hydrogen across the top and bottom faces in all the different models of the hydrogen transport analysis described here. The finite element analysis is performed for each sample of

NPC material with synthetic microstructures containing different grain sizes, different volume fraction of TJs, different shape of TJs, nano fine grains in TJs, pores in TJs and also for a single crystal material. The hydrogen diffusion coefficients of electrodeposited nickel used for the three different phases of the microstructures are diffusivity of GI (D_{GI}) =2.9*10^{-8} cm^2/s, diffusivity of GBAZ (D_{GBAZ}) =6.3*10^{-9} cm^2/s and diffusivity of TJ (D_{TJ}) =2.1*10^{-10} cm^2/s [1]. The synthetic microstructure model containing nano fine grains in TJs is modelled by dividing the TJs of the three-phase synthetic microstructural model into fine grains with an average grain size of 1 nm. The effective diffusivity of the fine nano grains is assumed to be 1×10^{-8} cm^2/s [8, 47]. Mesh sensitivity studies were performed for all samples and then sufficient elements were used in the GI, GBAZ and TJ to capture the time evolution of hydrogen concentration in the NPC nickel. Figure 4 shows the statistical distribution of elements per grain interior for the GBAZ in the synthetic mesoscale microstructural model of NPC material. This shows that the average number of elements in each grain was 6000 and average number of elements in each GBAZ was 400. Figure 5 shows the statistical distribution of the number of elements per TJ in synthetic microstructural models for sharp corner TJs and round corner TJs. This shows an average number of 50 elements per TJ in the sharp corner TJ synthetic microstructural model and an average number of 400 elements per TJ in the round corner TJ synthetic microstructural model. The difference in the average number of elements per TJ between the sharp corner TJ and round corner TJ microstructure is due to the increase in the area fraction between them. Figures 4 and 5 show the number of elements that are placed in the three different phases of the three phase synthetic microstructural model to capture the hydrogen transport concentration in NPC material. Figure 6 shows the discretization nodes of the sharp corner TJ three phase synthetic microstructural models and finite element (FE) mesh of the model in a region with TJs, GBAZs and three adjacent neighbouring grains of NPC material. Hydrogen transport algorithms used in these computational experiments are based upon Fick's diffusion laws applied using finite element method. The transport of hydrogen is described by Fick's law from the high concentration region to low concentration region based on the standard equations shown below.

$$\overline{J_c(X,t)} = -D \cdot \nabla C \cdot = -D \cdot \left(\frac{\partial C(x,t)}{\partial x} + \frac{\partial C(y,t)}{\partial y}\right) \cdot \quad (1)$$

$$\overline{J_c(X,t)} = -D \cdot \frac{\partial C(X,t)}{\partial X} \cdot \quad (2)$$

The hydrogen flux vector $\overline{J_c}$consists of the hydrogen concentration gradient $\boldsymbol{\nabla C}$ at a specific time *t* based on *Fick's first diffusion law* by using the *thermodynamic formulation* based on the *Gibbs free enthalpy*. The diffusivity *D* (D_{GI} *or* D_{GBAZ} *or* D_{TJ}) depends on the phase in the NPC material. The NPC synthetic microstructural model consists of three phase heterogeneous GI, GBAZ and TJs similar to the modelling procedure of two phase microstructure explained in detail elsewhere [8] with the inclusion of third phase as TJs as shown in Figure 3. The material properties of the microstructural model are considered as following, Concentration of hydrogen *C*, gradient operator$\boldsymbol{\nabla}$, Laplace operator $(\boldsymbol{\nabla}.\boldsymbol{\nabla})$ **or** $\boldsymbol{\nabla^2}$ ***or*** Δ, *X* represents two dimension (2D) *x,y* directions for simplification. The commercial software ABAQUS implements the above diffusion equation as shown in equation (3) [13].

$$\overline{J_c(X,t)} = -sD \cdot \frac{\partial \phi(X,t)}{\partial X} \cdot \qquad (3)$$

Where solubility *s*, $\phi = C/s$ is the normalized hydrogen concentration.

Detailed information about the numerical method to solve the governing diffusion equation can be found in elsewhere [10, 13].

3. Results of computation and discussions:

3.1 Results of computationally developed mesoscale microstructural models of NPC material with different grain sizes and volume fraction of TJs:

For computational calculation of hydrogen transport realistic mesoscale microstructures are modelled for three different average grain sizes 50 nm, 10 nm and 5 nm of NPC materials as shown Figure 7 (a), (b) and (c). Figure 7 (d) is a radar triangle graph showing the effects of average grain size of NPC material on the calculated volume fraction of GI, Ig, GBAZ and TJ from the computed microstructures of average grain sizes 5 nm, 10 nm and 50 nm. The volume fraction of the intergranular region increases by one order of magnitude as the average nano grain size decreases from 50 nm to 5 nm. At the same time when decreasing the average nano grain size from 50 nm to 5 nm the volume fraction of GI decreases from 92.12 % to 35.65 %, with the major decrease in volume fraction of 45 % from 80.87 % occurring when decreasing the grain size from 10 nm to 5 nm as shown in table1. The result of the computationally developed synthetic NPC material shows that the decrease in average size from 50 nm to 10 nm increases the volume fraction of TJ by one order of magnitude with less than 1 % increase in the density of TJ of NPC material from

0.16 %. A decrease in the average grain size from 10 nm to 5 nm increases the volume fraction of TJ by 15.12 % from 1.03 %. The decrease in average grain size of NPC material from 50 nm to 5 nm increases the volume fraction of TJ by 2 orders of magnitude, increases the volume fraction of GBAZ by one order of magnitude and decreases the volume fraction of GI by less than one order of magnitude. Palumbo [2] found a similar trend relating the volume fraction and density for TJ with changes in nano grain size in 3D NPC materials.

Grain Size in nm	Volume fraction of GI	Volume fraction of TJ
5	35.65 %	16.18
10	80.87 %	1.03 %
50	92.12 %	0.16 %.

Table 1: Calculated volume fractions of GI and TJ from computationally developed synthetic mesoscale nanopolycrystalline models for three different grain sizes.

3.2 Results of the effects of TJ with respect to grain size and volume fraction of TJs in hydrogen transport of NPC material:

The effect of TJs on the hydrogen transport of electrodeposited NPC nickel are investigated using computationally developed NPC materials with synthetic microstructures (of average grain size 5nm, 10nm, 50nm and single crystal) by implementing the diffusivity values of TJ, GBAZ and GI from Palumbo et al [1]. The results of these analyses for the three different average grain sizes and a single crystal of NPC material, all with the same domain area of 2.5 nm^2 and at temperature 298 K, are shown in Figure 8 after three different time periods 1.3, 83 and 167 ms. The results show that hydrogen transport after 1.3 ms in 50 nm grain size NPC material is slower than that for the 10 nm average grain size at the same time in the same domain. The hydrogen transport in the bulk microstructure of 5 nm grain size NPC material is more than twice as fast as the NPC material with a grain size of 10 nm and much faster than the 50 nm grain size NPC materials. The much faster bulk hydrogen transport in NPC material of 5 nm grain sizes when compared to 50 nm is due to the 16 % higher volume fraction of TJ between the 50 nm and 5 nm grain size microstructures. The hydrogen transport in 5 nm grain size NPC material attains steady state earlier than 83 ms and the 10 nm grain size NPC material attains steady state at 163 ms, but the 50 nm grain size NPC material does not attain steady state even after 167 ms. Since the diffusivity of the TJs is higher and the area density of the TJ is also higher in the 5 nm grain size structure the hydrogen diffuses much faster in 5nm grain size structure than the 10nm grain size structure

and the hydrogen diffusion in 5nm grain size structure attains steady state much earlier than the 50nm grain size structure. The results clearly show that a major increase in the density of TJs is found when the average grain size is less than or equal to 10nm in NPC materials. This transports the hydrogen in bulk NPC material much further and faster attaining steady state much earlier than the microstructure of NPC material with an average grain size greater than 10 nm. Since the TJ plays a vital role in NPC material of 10 nm and less than 10 nm, it is important to consider the effects of TJs on NPC material with hydrogen embrittlement problems experimentally as well as via modelling. Figure 9 shows the results of the computed dimensionless hydrogen concentration for various different volume fractions of TJs for three different times and two different positions in NPC materials. Figure 9 show that an increase in the volume fraction of TJs increases the accumulation of hydrogen concentration in the NPC material.

Figure 10 shows how the normalized hydrogen concentration varies with time for various grain sizes and the single crystal material. The hydrogen transport in the single crystal material is slower than the hydrogen transport in NPC material. The normalized hydrogen concentration is smaller in microstructures with average grain sizes of 50 nm and higher compared to the 5 nm NPC material. This effect is due to the lower volume fraction of TJ in higher grain size NPC material. Figure 11 shows how the normalized concentrations depend on the normalized distance for various average grain sizes and single crystal material. The area under the normalized hydrogen concentration curves increases from single crystal material to smaller grain sizes. These increases are due to the increase in the volume fraction of the TJs as the grain size decreases in the NPC material. The difference in the area under the normalized concentration curve (i.e. the total normalised accumulated hydrogen within the samples) is greatest between the 5nm vs 10nm case compared to the difference in the area under the normalized concentration curve between the 10nm vs 50nm and the single crystal vs 50nm cases. This is because the increase in the volume fraction of TJs is higher when the grain size is less than 10nm.

3.3 ***Results of computationally developed mesoscale microstructural models for sharp and round shape corner TJ:***

Two different types of TJs are absorbed in real microstructure of polycrystalline nickel material with same average grain size as shown in figure 12 (a) and (d) (i.e figure 12 (a) sharp corner TJ and figure 12 (d) round corner TJ). So, we developed two different types of synthetic mesoscale microstructures with the same average grain size. One with sharp corner

TJs and another with round corner TJs. Figure 12 (b) show the close view of mesoscale synthetic microstructure with sharp corner TJ and figure 12 (c) shows the close view of developed mesoscale microstructure with round corner TJ. From the geometry of the mesoscale microstructural model for the two different TJ shapes, the statistical distribution of the grain area and the GBAZ area are computed and shown in Figure 13 (a) and (b) respectively. The mean values of the average grain area distribution are 34.8 nm^2 and the average GBAZ area distribution is 2.7 nm^2 as computed from Figure13 (a) and Figure13 (b) respectively. Figure14 (a) and (b) shows the computed statistical area distributions for the sharp corner TJs and round corner TJs. The total area of TJ in the 'round corner TJ' (187.14 nm^2) mesoscale model is approximately seven times higher than the 'sharp corner TJ' (25.92 nm^2).

The average grain size between the round corner TJ mesoscale model and sharp corner TJ mesoscale model are the same but the area fractions of TJ in these two models is different. This difference in the area fraction of TJ is due to the change in the shape of the TJ. The mean values of both of these TJ area distributions are computed as 0.2477 nm^2 and 2.552 nm^2 respectively. The mean area value of the sharp corner TJ is one order of magnitude higher than the round corner TJ microstructure of NPC material. Figure14 (a) shows the computed statistical distribution of the GBAZ thickness and its computed mean value is 0.6957 nm. Figure 15 (b) shows the cumulative frequency of the TJ area distribution between sharp corner TJs and round corner TJs. Only 25% of the TJs are greater than 3.5nm^2 in the round corner TJ microstructural model and less than 1% of TJs are greater than 0.5nm^2 in the sharp corner TJ microstructural model. The change in the shape of the TJ is due to the presence of higher number of disordered atom in and around the triple junctions. The cross section of round corner TJ considered in this analysis is similar to the cross section of TJ used by Wang in his work as shown in figure 1(a) [20].

3.4 ***Results of the effects of TJ shape in hydrogen transport of NPC material:***

Figure 16 shows the results of the computational analysis of hydrogen transport in mesoscale microstructures with sharp corner TJs and round corner TJs after two different time periods of 2.6 ms and 20.97 ms in the same domain with the same grain size and with the same material diffusivity properties. The hydrogen transport is accelerated in the round corner shape TJ microstructure NPC material as compared to the sharp corner shape TJ microstructure. This acceleration of hydrogen transport in round corner TJ NPC material is associated with the higher relative volume fraction of TJs. Figure 17 shows the normalized

hydrogen concentration calculated at TJs as a function of time for three different distances X1 (15.21) , X2 (32.92) and X3 (51.80) for the sharp corner TJ and round corner TJ models. In all of the three different distance cases the size and shape of the TJs affects the hydrogen transport. The decline in the area under the curve of the normalized hydrogen concentration in the sharp corner shape TJ microstructure when compared to the round corner TJ microstructure is due to the reduction in the density of TJs in the sharp corner TJ microstructure. Figure 18 shows how the computed normalized hydrogen concentration depends on normalised distance with the same average grain size having two different volume fractions of TJ. The graph was plotted after 10 ms of hydrogen diffusion in the sample material. The 0.064 increase in volume fraction of TJ microstructure increases the area under the curve of normalized hydrogen concentration (the total normalised accumulated hydrogen with in the sample). This demonstrates how an increase in the volume fraction of TJ (associated with much higher diffusion coefficients) enhances bulk diffusion of hydrogen.

3.5 *Results of the effects of pores and fine grains in TJs of hydrogen transport of NPC material:*

Results for the synthetic microstructures with nano fine grains in TJ and voids in TJ are shown in the Figure19 (a) and (c) respectively. Figure19 (b) shows the material with pores in the TJs taken from Bokstein et al [5] and Figure 19 (c) shows the microstructure of NPC material developed based on the Bokstein schematic model of NPC material with pores in the TJs [5]. The volume fraction of void considered in the model is 0.186. In the three phase (Ig, GBAZ and TJ) synthetic microstructure model, the TJs are further divided into fine grains with an average grain size of 1 nm. The microstructures with fine grains in TJs and voids in TJs were investigated with respect to hydrogen transport. The results of hydrogen transport analyses of material with nano fine grain microstructure in TJs and voids in TJs for various time periods are shown in Figure 20. The 2 dimensional hydrogen transports in a microstructure with fine grains in TJs is faster than the NPC microstructure with voids in TJs. Therefore it is important to take into account microstructural features such as voids, fine grains etc… in TJs to correctly capture the hydrogen transport in NPC material. Figure 21 shows how the computed normalized hydrogen concentration depends on time for 10nm grain size material with three different microstructures (material with microstructure containing TJs, fine grains in TJs and pores in TJs). The area under the curve is greater for microstructures with normal TJs than those containing fine grains in TJs and pores in TJs. The area under the curve is smaller for microstructures containing pores in TJs than the

microstructure with fine grans in TJs and microstructure with normal TJs. These results show that the bulk diffusion of hydrogen in NPC material with microstructures containing fine grains in TJs is slower than the microstructure with normal TJs and faster than the microstructure with pores in TJs.

3.6 The effects of presence/absence of TJs in hydrogen diffusion in NPC material:

Figure 22 shows how the computed normalised hydrogen concentration depends on the normalized distance (Y/Yt) at a distance (X/Xt)=0.65 in the x-direction for 10nm grain size NPC material with a two phase microstructure (GI and Ig phases) without TJs and a three phase microstructure (GI, GBAZ and TJ phases) with TJs. The diffusivity value used for Ig was 6.3×10^{-9} cm^2/s. In the three phase microstructure the TJ is considered as a separate phase. The hydrogen transport in these two phase and three phase microstructures is heterogeneous due to the difference in the hydrogen transport properties of microstructural GI, GBAZ, Ig, and TJ. It is interesting to note that the two curves for normalised concentration with and without TJs in Figure 22 would almost overlie one another if the lower curve was moved upwards. This highlights that the main effect is increased flow rates within TJs compared to the Ig phase. Figure 22 also shows the computed homogenous normalised hydrogen concentration at the same place in a single crystal. The hydrogen transport in single crystal nickel is both slower than the NPC nickel and homogenous. For better understanding of the accumulation of hydrogen in TJs in NPC nickel the graph is plotted for accumulated normalized hydrogen concentration depending on the number of TJs in the three phase microstructure and on Ig in the two phase microstructure along the path at a normalised distance of (X/Xt) 0.045 at time 0.164ms in figure 23. The accumulation of hydrogen is higher in TJs of the two phase NPC nickel when compared to the accumulation of hydrogen in Ig for the three phase microstructure. This also demonstrates that the accumulated hydrogen in TJs and Ig are heterogeneously distributed even along the same path. These results show that the hydrogen concentration in the three phase microstructure is higher than the two phase microstructure due to the faster transport of hydrogen in the three phase microstructure containing the TJs. Figure 23 also shows that even at a very small distance from the left-hand side there is a difference between a model with TJs and a model without TJs. Thus the TJ significantly affects hydrogen transport with the accumulation of hydrogen being heterogeneous. This reinforces the importance of considering TJs in modelling as well as experimental observations when investigating hydrogen transport in NPC nickel.

4. Conclusion:

Hydrogen transport in NPC nickel is complicated and depends on specimen microstructural morphology such as the presence of a high density of TJ, residual pores in TJs and fine grains in TJs. This work demonstrates the effects of microstructural morphology and especially TJs on the hydrogen transport response in NPC nickel.

1. The present work has shown that the hydrogen diffusion in NPC nickel is enhanced when
   - grain size get smaller
   - the volume fraction of TJs increases,
   - the TJs change shape from 'sharp corner' to 'round corner'
   - fine nano grains are present in TJs
2. The present investigation shows that the presence of pores in TJs slows down the bulk diffusion of hydrogen in NPC material and the pores may also act as trap sites for hydrogen.
3. In the model hydrogen diffusion in single crystal nickel is homogenous and slower than NPC nickel.
4. Finally, specimens with two phase (GI, Ig) microstructure and three phase (GI, GBAZ, TJ) microstructure NPC were investigated. The hydrogen diffusion in TJ microstructures is faster than the hydrogen diffusion in Ig microstructures.

Even though the NPC nickel microstructure is complicated in nature, it is very important to consider the specimen's microstructural morphology in and around TJs and the effect of TJs in order to understand hydrogen transport in NPC nickel via modelling as well as via experiment, especially with grain sizes of 10 nm and below.

Acknowledgements:

This work was supported by the MultiHy Project funded by the European Union's 7th Framework program under the theme "Nanosciences, Nanotechnologies, Materials and new production Technologies".

References:

[1] G.Palumbo, D.M.Doyle, A.M.El-Sherik, U.Erb and K.T.Aust (1991) Intercrystalline hydrogen transport in nanocrystalline nickel, Scripta METALLURGICA et MATERIALIA 25:679-684.

[2] G.Palumbo, S.J.Thorps and K.T.Aust (1990) On the contribution of triple junctions to the structure and properties of nanocrystalline materials, Scripta METALLURGICA et MATERIALIA 24:1347-1350.

[3] Y.Chen and C.A.Schuh (2007) Contribution of triple junctions to the diffusion anomaly in nanocrystalline materials, Scipta Materialia 57:253-256.

[4] B.S.Bokstein, H.D.Brose, L.I.Trusov, T.P.Khvostantseva (1995) Diffusion in Nanocrystalline nickel, NanoStructures Materials, 6:873-876.
[5] Lingling Hu, Ruxiao Huo, Jianqiu Zho, Ying Wang and Shu Zhang (2012) The effects of the finest grains on the mechanical behaviours of nanocrystalline materials, J Nanopart Res, 14:677.
[6] W.Bollmann (1998) Philos. Mag. A, 57:637.
[7] M.A.Meyers, E.Ashworth (1982) A model for the effect of grain size on the yield stress of metal, Phil. Mag. A46:737.
[8] Jothi, S., Croft, T.N., Brown,S.G.R. and de Souza Neto, E. (2014) Finite Element microstructural homogenization techniques and intergranular, intragranular microstructural effects on effective diffusion coefficient of heterogeneous polycrystalline composite media., Composite Structures 108: 555-564.
[9] David J. Benson, Hsueh-Hung Fu, Marc Andre Meyers (2001) On the effect of grain size on yield stress: extension into nanocrystalline domain, Materials science and Engineering A319-321:854-861.
[10] Jothi,S., Croft, T.N., Brown,S.G.R. and de Souza Neto, E. (2013) Computational analysis of hydrogen diffusion in polycrystalline nickel and irregular polygonal micro and nano grain size effects, Proceedings of the 5th International conference on Hydrogen safety, Brussels, 9-11 September.
[11] H.Margolin (1998) Polycrystalline yielding-perspectives on its onset, Acta Mat. 46:6305-6309.
[12] A.P.Sutton, R.E.Baluffi (2006) Interfaces in Crystalline Materials, Oxford University Press.
[13] ABAQUS 12. tutorial manual
[14] M. R. Chellali, Z. Balogh, H. Bouchikhaoui, R. Schlesiger, P. Stender, L. Zheng and G. Schmitz (2012) Triple Junction transport and the impact of grain boundary width in nanopolycrystalline Cu, Nano Lett. 12: 3448-3454.
[15] A. Portavoce, L. Chow and J. Bernardini (2010) Triple junction contribution to diffusion in nanocrystalline Si, Applied physics Letters 96: 214102.
[16] A. Portavoce, G. Chai, L. Chow and J. Bernardini (2008) Nanometric size effect on Ge diffusion in polycrystalline Si, Journal of Applied Physics 104:104910.
[17] H. Gleiter (1989) Nanocrystalline materials, Progress in Materials Science 33:223-315.
[18] B. Bokstein, V. Ivanov, O. Oreshina, A. Peteline and S. Peteline (2001) Direct experiemental observation of accelerated Zn diffusion along triple junctions in Al, Mate Sci Eng A302:151-153.
[19] I.M. Mikhailovski, V. B. Rabukhin, O. A. Velikodnaya (1991) On the enchancement of the diffusion permeability near triple junctions, Phys status Solidi A 125:K65.
[20] H. Wang, W. Yang, A.H.W. Ngan (2005) Enhanced diffusivity by triple junction networks, Scripta Materialia 52:69-73.
[21] L. M. Klinger, L.A. Levin and A.L. Peteline (1997) The model of triple junction diffusion, Defect and Diffusion Forum 143-147:1523-1526.
[22] A. Vinogradov and S. Hashimoto (1997) Effects of triple junction on fatigue crack growth in copper and copper -3AT.% aluminium tricrystals, Scripta Mater. 36:417-423.
[23] N.Wang, Z. Wang, K.T. Aust and U. Erb (1995) Effect of grain size on mechanical properties of nanocrystalline materials, Acta Metallurgica et Meterialia 43:519-528.
[24] C. R. Chen, S. X. Li, J. L. Wen, W. P. Jia (2000) Finite element analysis about effects of stiffness distribution on stresses and elastic strain energy near the triple junctions in a tricrystal, Materials Science and Engineering A282:170-176.

[25] L. Lu, M.L. Sui and K. Lu (2000) Superplastic extensibility of nanocrystalline copper at room temperature, Science 287:1463-1466.
[26] Z.B. Wang, N.R. Tao, W.P. Tong, J. Lu and K. Lu (2003) Diffusion of chromium in nanocrystalline iron produced by means of surface mechanical attrition treatment, Act Materialia 51:4319-4329.
[27] T. Frolo and Y. Mishin (2009) Molecular dynamics modelling of self-diffusion along a triple junction, Phy. Rev. B 79:174110.
[28] Y. Zhou, G. Palumbo, K.T. Aust and U. Erb (2013) Triple junction structure and carbide precipitation in 304L stainless steel, Journal of Materials Research 28:1589-1600.
[29] J. Schiotz, F.D.D. Tolla and K.W. Jacobsen (1998) Softening of nanocrystalline metals at very small grain sizes, Nature 391:561-563.
[30] M.A. Meyers, A. Mishra and D.J. Benson (2006) Mechanical properties of nanocrystalline materials, Proess in Materials Science 51:427-556.
[31] Z. Balogh, C. Oberdorfer, M.R. Chellai, P. Stender, S. Nowak and G. Schmitz (2013) Defect analysis by statistical fitting to 3D atomicmaps, Ultramicroscopy 132:86-91.
[32] D. Prokoshkina, V.A. Esin, G. Wilde and S.V. Divinski (2013) Grain boundary width, energy and self-diffusion in nickel: Effect of material purity, Acta Materialia 61:5188-5197.
[33] Z. Balogh, P. Stender, M.R. Chellali and G. Schmitz (2013) Investigation of interfaces by atom probe tomography, Metallurgical and Materials Transactions A44:4487-4495.
[34] A. Caro and H. Van Swygenhoven (2001) Grain boundary and triple junction enthalpies in nanopolycrystalline metals, Phys. Rev. B 63:134101.
[35] P. Stender, Z. Balogh and G. Schmitz (2011) Triple junction segregation in nanocrystalline multilayers, Phys. Rev. B 83:121407.
[36] M.R. Chellai, Z. Balogh, L. Zheng and G. Schmitz (2011) Triple junction and grain boundary diffusion in the Ni/Cu system, Scr. Mater. 65:343-346.
[37] A.M. El-Sherik and U. Erb (1994) Production of Nanocrystalline Metals, US Patent No.,5, 352, 266.
[38] http://cs.astrium.eads.net/sp/launcher-propulsion/rocket-engines/vulcain-rocket-engine.html (last accessed 15/October/2013).
[39] A.M. El-Sherik, U. Erb and J. Page (1996) Microstructural evolution in pulse plated nickel electrodeposits, Surface and Coating Technology 88:70-78.
[40] L, Klinger, I. Gotman and E. Rabkin (2013) A mesoscopic model of dissolution/disintegration of nanocrystalline meals via vacancy diffusion along grain boundaries, Computational Materials Science 76:37-42.
[41] L. Klinger and E. Rabkin (2011) Theory of the Kirkendall effect during grain boundary interdiffusion, Acta Materialia 59:1389-1399.
[42] L. Klinger, E. Rabkin, L.S. Shvindlerman and G. Gottstein (2008) Grain growth in porous two dimensional nanocrystalline materials, J Mater Sci 43:5068-5075.
[43] Y. Chen and C.A. Schuh (2007) Geometric considerations for diffusion in polycrystalline solids, Journal of Applied Physics 101:063524.
[44] L. Klinger, E. Rabkin, L.S. Shvindlerman and G. Gottstein (2008) Grain growth in porous two dimensional nanocrystalline materials, J Mater Sci 43:5068-5075.
[45] A. Alvaro, V. Olden and O.M. Akselsen (2013) 3D cohesive modelling of hydrogen embrittlement in the heat affected zone of an X70 pipeline steel, International journal of hydrogen energy 38:7539-7549.
[46] V. Olden, C. Thaulow and R. Johnsen (2008) Modelling of hydrogen diffusion and hydrogen induced cracking in supermartensitic and duplex stainless steels, Materials and Design 29:1934-1948.

[47] A. Oudriss, J. Creus, J. Bouhattate, E. Conforto, C. Berziou, C. Savall, X. Feaugas (2012) Grain size and grain boundary effects on diffusion and trapping of hydrogen in pure nickel, Acta Materialia 60:6814-6828.

[48] Jothi, S., Croft, T.N., Brown,S.G.R. (2014) Influence of grain boundary misorientation on hydrogen embrittlement in bi-crystal nickel., Int J hydrogen Energy, (In press) DOI: 10.1016/j.ijhydene.2014.07.020.

[49] MATLAB Tutorial manual

Modelling the Influence of Microstructural History and Triple Junctions on Hydrogen Transport in Nanopolycrystalline Nickel

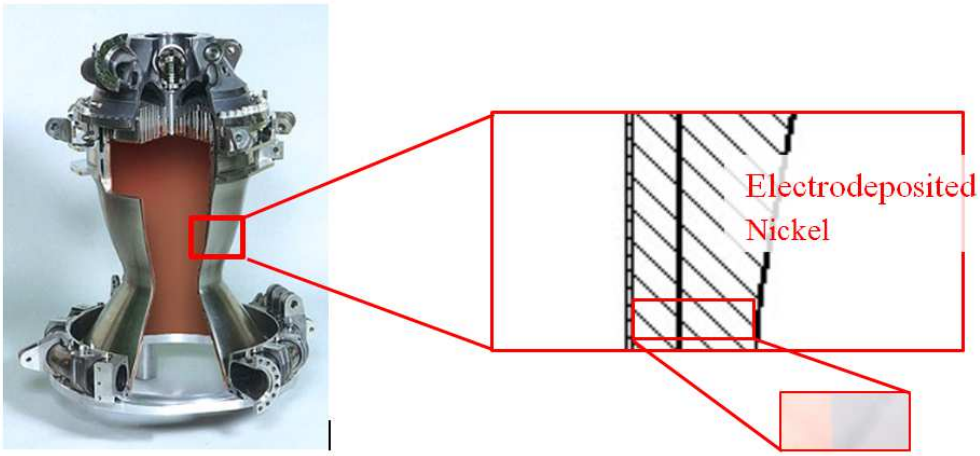

Fig. 1 Electrodeposited nickel used in the Ariane space shuttle [38].

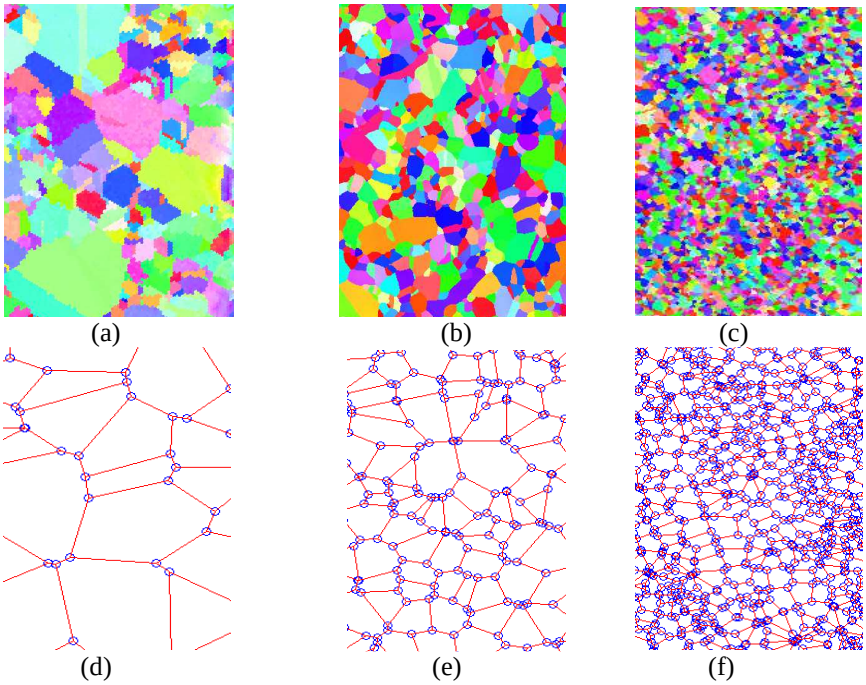

Fig. 2 (a), (b) and (c) are the 2D EBSD (Electron backscattered diffraction) experimental microstructural image of NPC Nickel with decrease in average grain sizes respectively. The decrease in average grain size shows the increase in number of triple junctions. Fig. 2 (d), (e) and (f) are the schematic views of two dimensional multiphase NPC model showing the increased number of triple junctions in NPC material as the grain sizes decreases. The blue circles, red lines and white polygons show the triple junction phases, grain boundary phases and grain phases respectively.

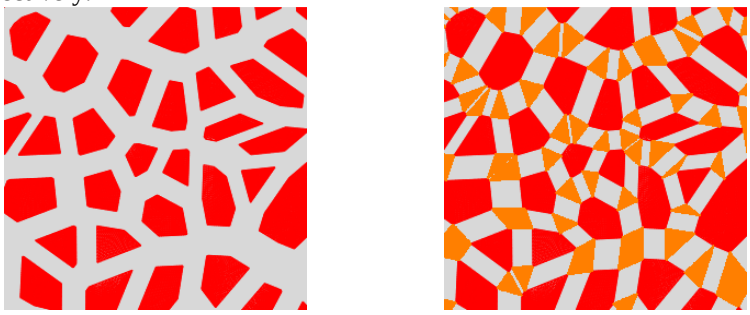

(a) (b)

Fig. 3 (a) Synthetically developed microstructural model for NPC material based on the modified double line Voronoi (i.e. this double line area is considered as microstructural Ig phase in the model) (b) Synthetic microstructural model based on modified three phase microstructural model (i.e. the double line Ig phase is divided into two region as GBAZ and TJ with sharp corners).

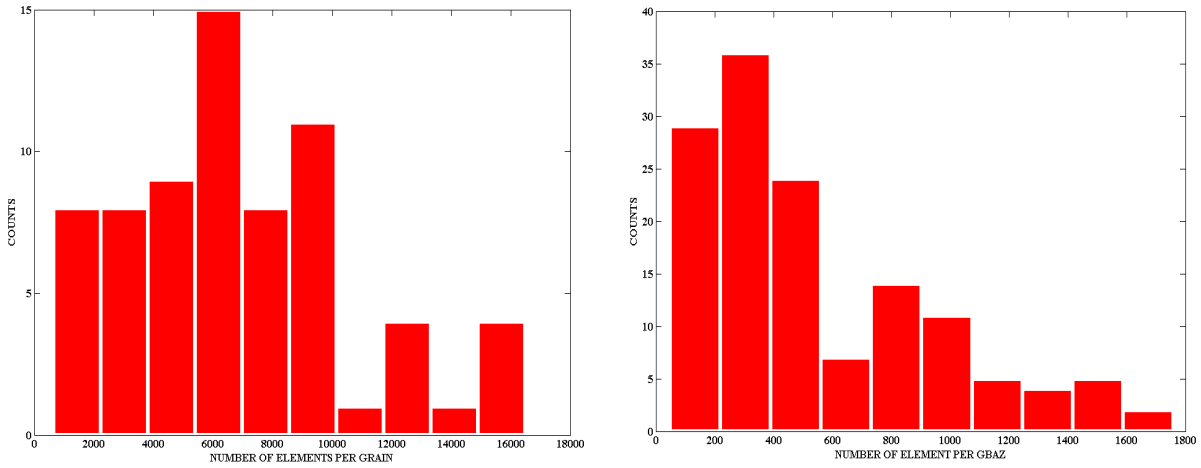

(a) (b)

Fig. 4 Statistical distribution of (a) the number of elements per grain and (b) the number of elements per GBAZ in a synthetic microstructure with the round cornered TJ model of NPC material.

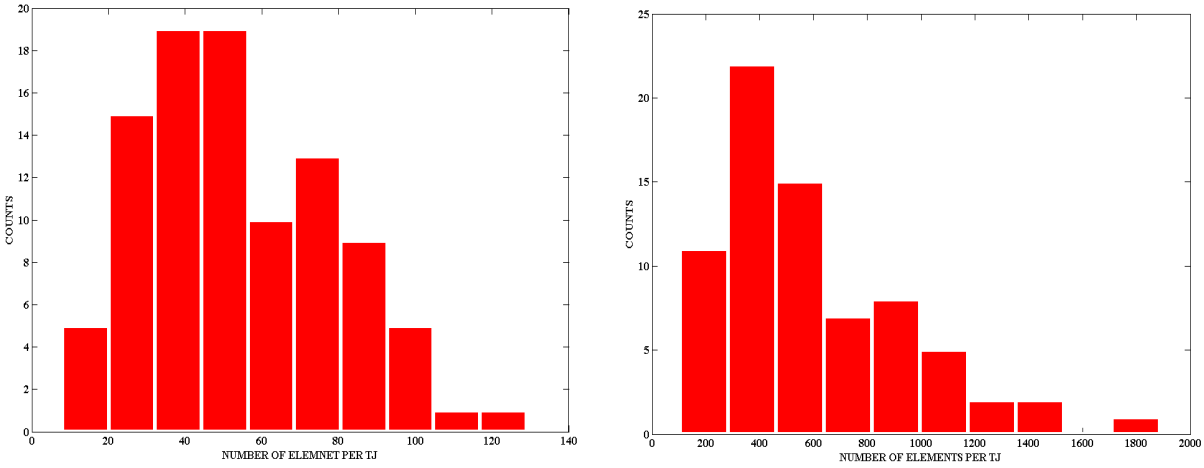

(a) (b)

Fig. 5 Statistical distribution of (a) the number of elements per TJ distribution of the sharp cornered TJ synthetic microstructural model and (b) the number of elements per TJ distribution of the round cornered TJ synthetic microstructural model of NPC material.

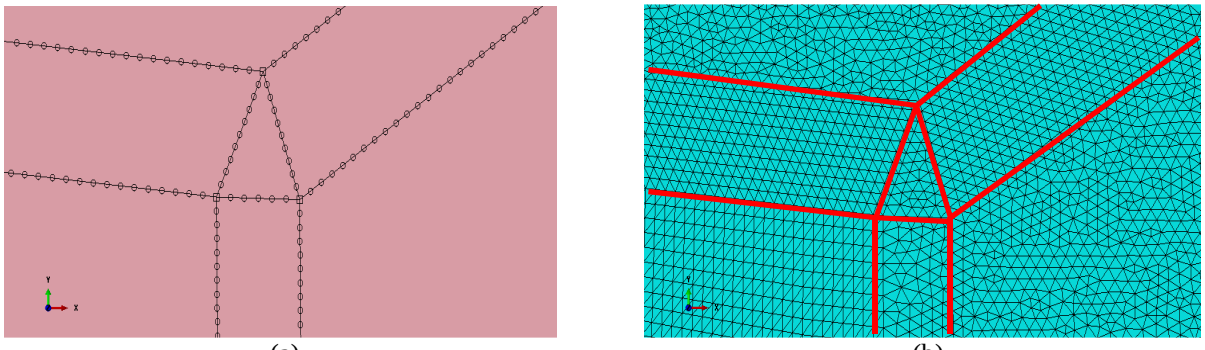

(a) (b)

Fig. 6 (a) Discretization nodes of the TJ with sharp corners, GBAZ and three neighbouring grains and (b) FE mesh of the same region as shown in the figure (a) of the NPC microstructural model.

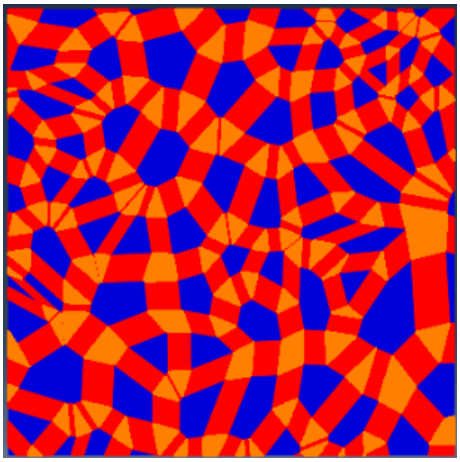

(a)

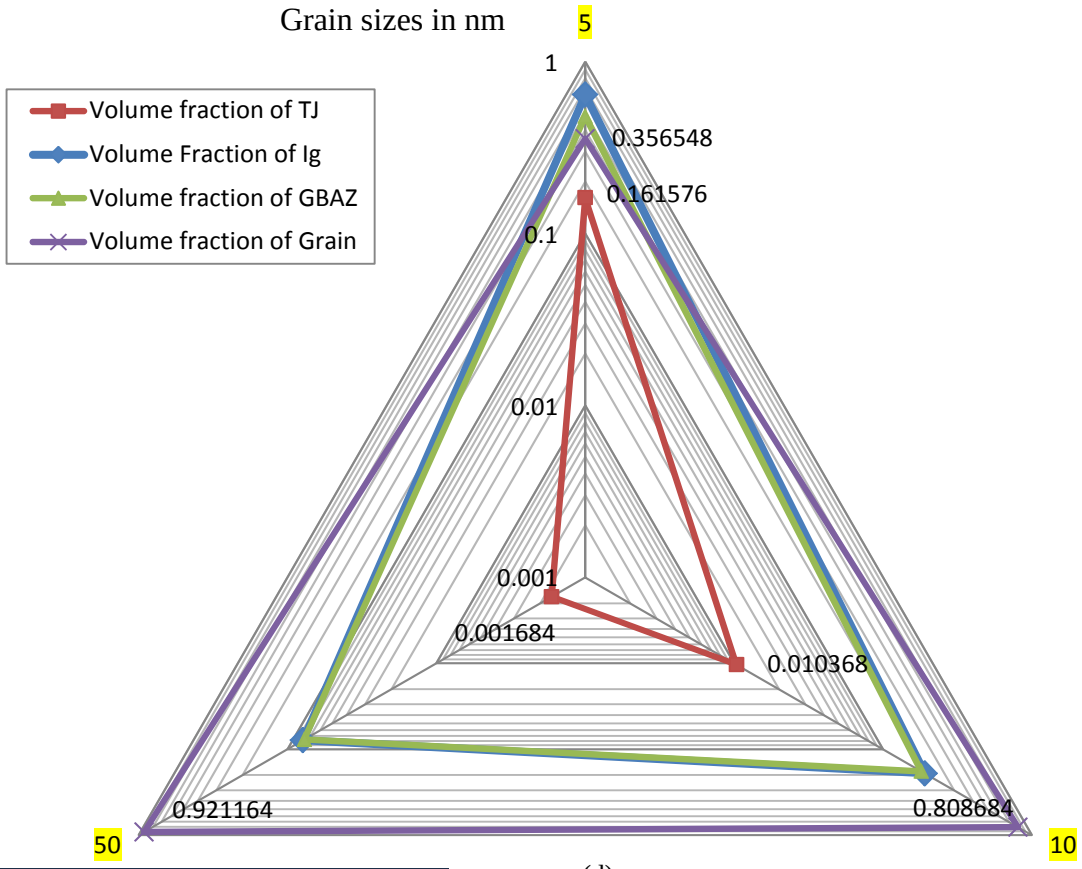
Grain sizes in nm
5
1
0.356548
0.161576
0.1
0.01
0.001
0.001684
0.010368
0.921164
0.808684
50
10
Volume fraction of TJ
Volume Fraction of Ig
Volume fraction of GBAZ
Volume fraction of Grain

(d)

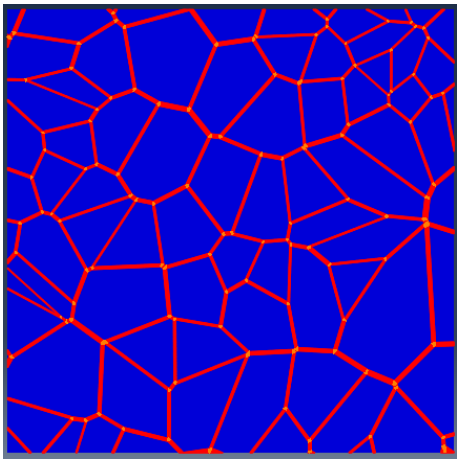

(c)

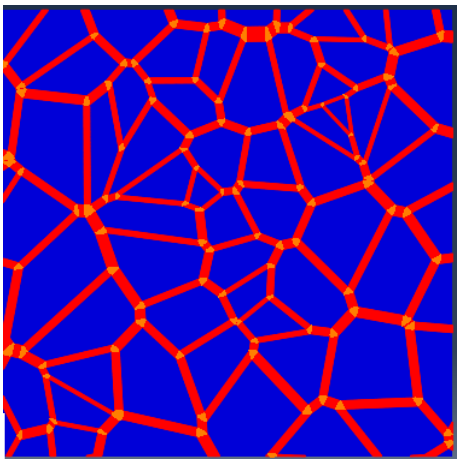

(b)

Fig. 7 Mesoscale microstructure of NPC material with average grain size of (a) 5nm, (b) 10nm and (c) 50nm. (d) A radar triangle graph showing the effect of average grain sizes of NPC materials on the calculated volume fraction of GI, Ig, GBAZ and TJ.

Grain size	**Time :1.3milliseconds**	**Time:83 milliseconds**	**Time: 167miliseconds**
Single Crystal	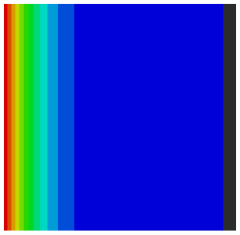	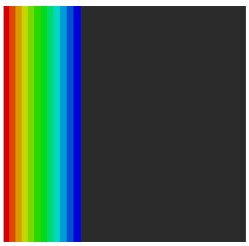	
50nm	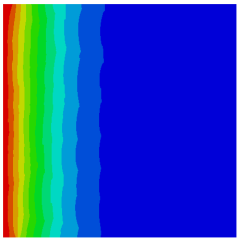		
10nm	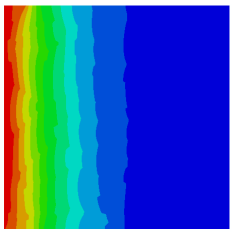		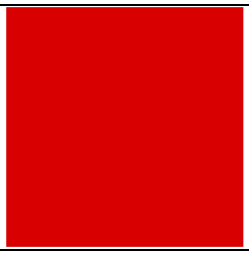
5nm	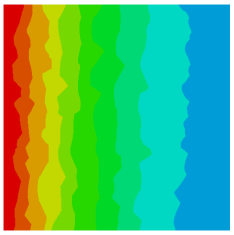		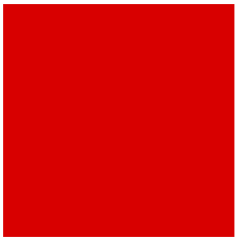
Coordinate Directions	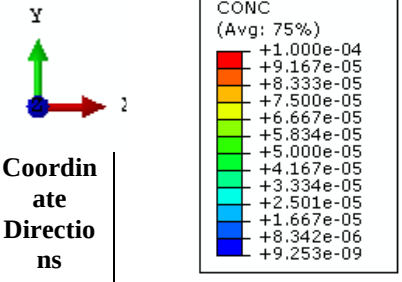	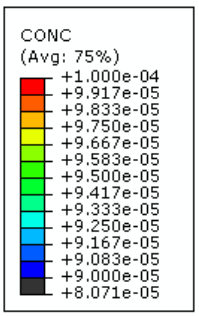	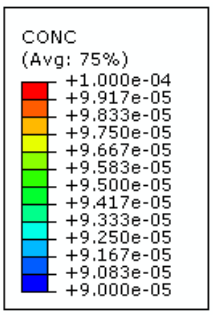

Fig. 8 Results of the hydrogen transport in mesoscale microstructures with average grain size of 5nm, 10nm and 50nm in NPC material after 1.3milisecond, 83milisecods and 167miliseconds.

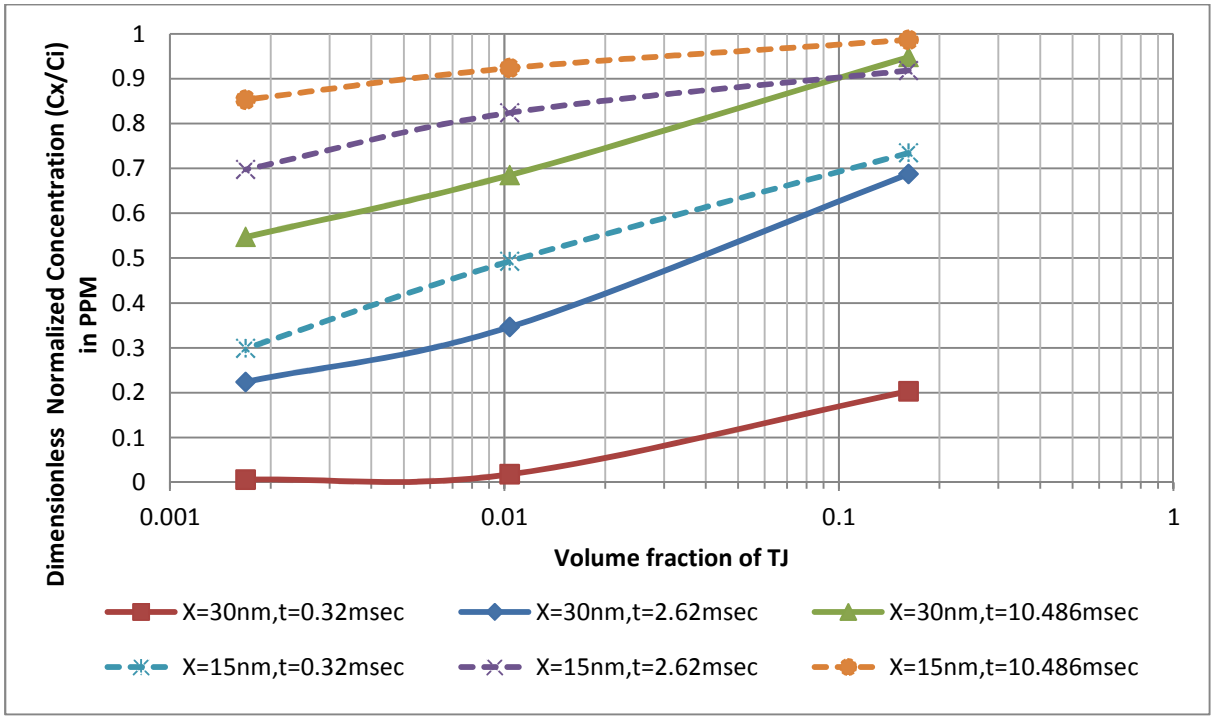

Fig. 9 Results of the computed dimensionless hydrogen concentration for three different volume fractions of TJs, three different times at two different positions in the NPC material.

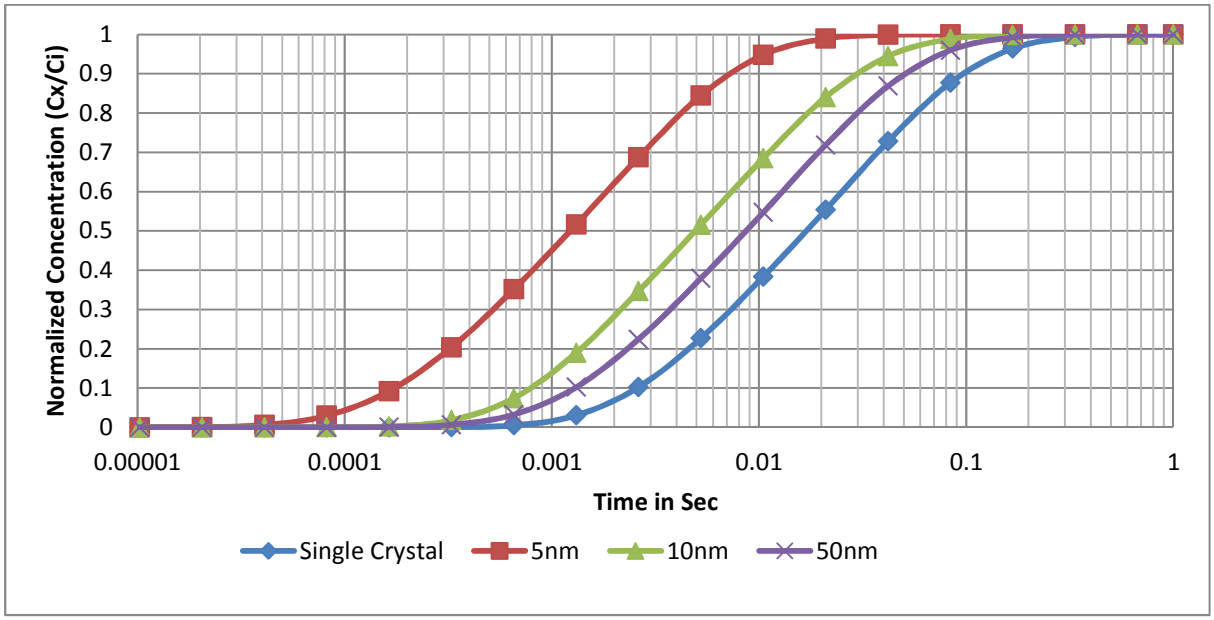

Fig. 10 Computed normalized hydrogen concentration dependency on time for various average grain sizes of 5 nm, 10 nm and 50 nm of NPC material and the single crystal case (the results have been calculated at X=30,0).

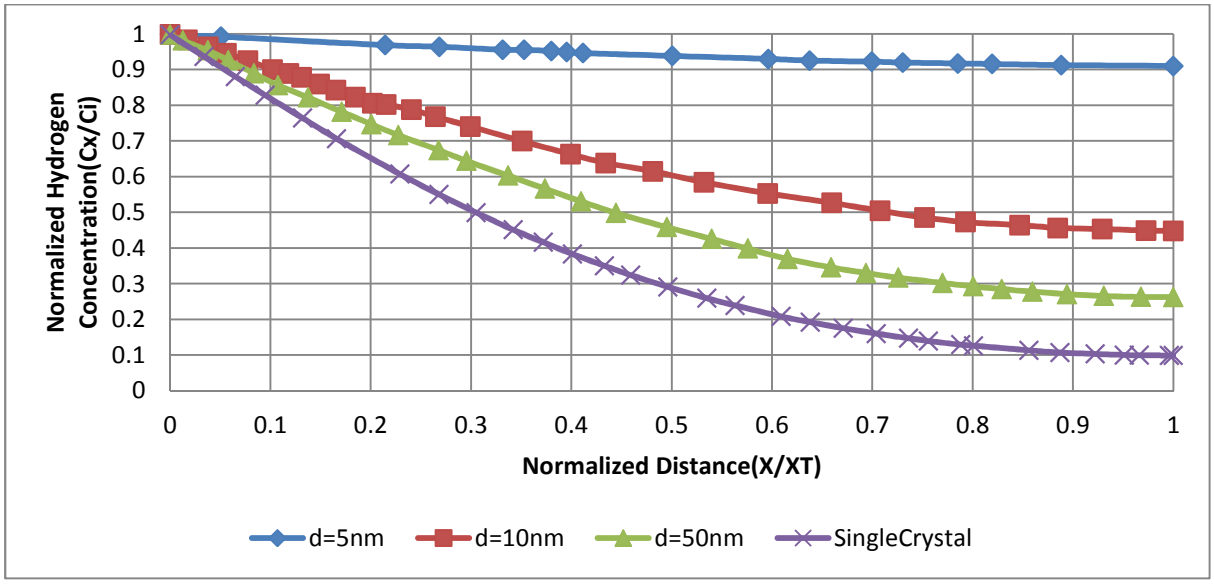

Fig. 11 Computed normalized hydrogen concentration dependency on normalized distance for various average grain size 5 nm, 10 nm and 50 nm NPC material and the single crystal material. The results have been calculated at time =10 ms.

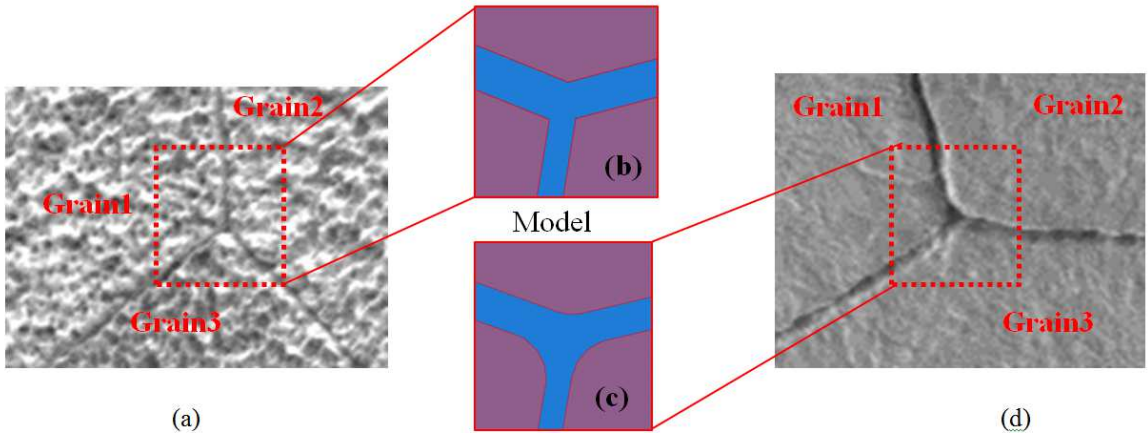

Fig. 12 Actual microstructures and models with two types of TJs. (a) real microstructure of nickel with 'sharp corner' TJ and (b) close up view of modelled 'sharp corner' TJ (c) close up view of modelled 'round corner' TJ and (d) real microstructure of nickel with 'round corner' TJ.

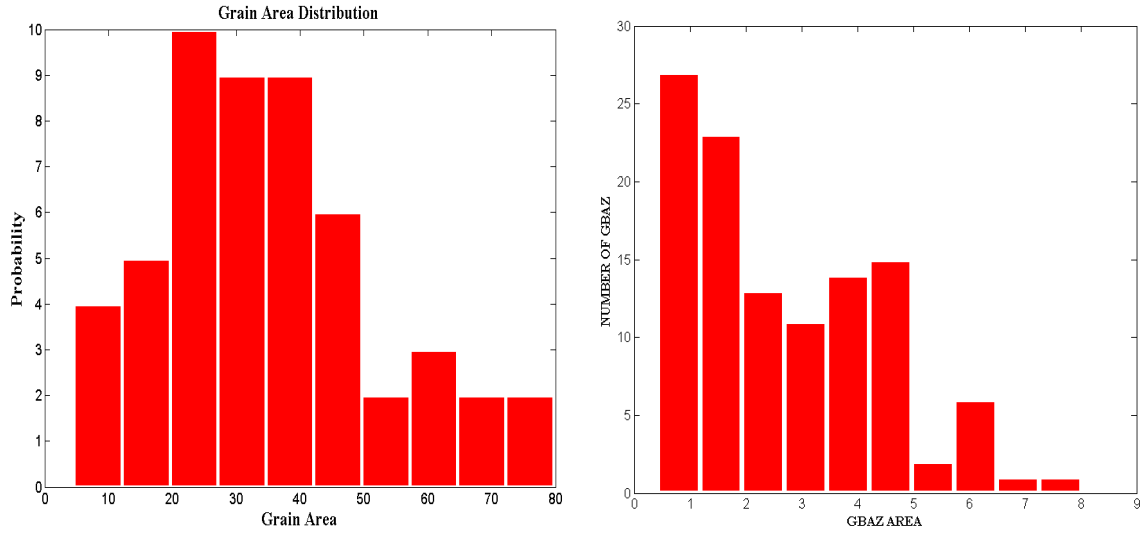

(a) (b)

Fig. 13 (a) Grain Area distribution and (b) GBAZ Area distribution of the Model

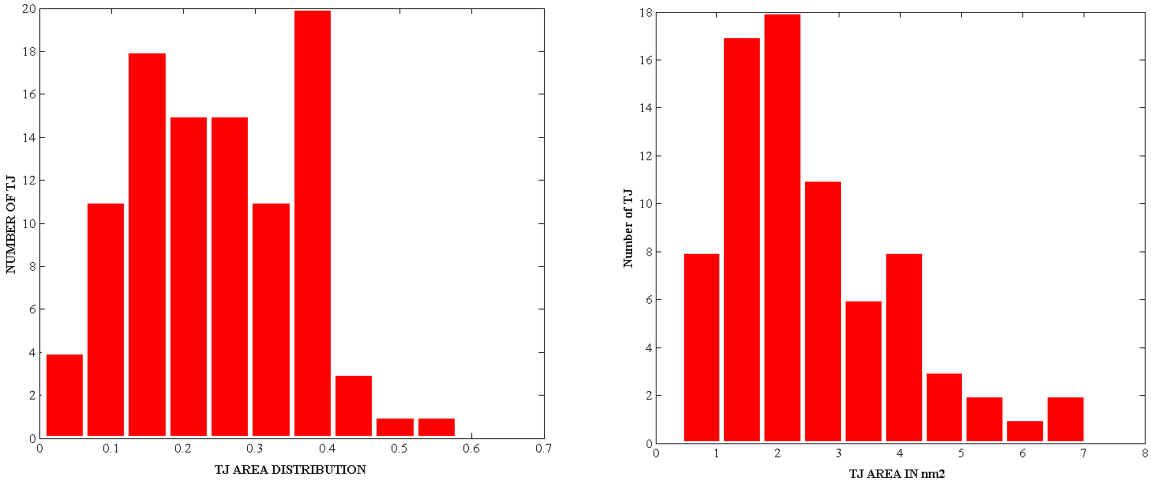

(a) (b)

Fig. 14 (a) TJ area distribution of the sharp corner TJ Model and (b) TJ area distribution of the round corner TJ model.

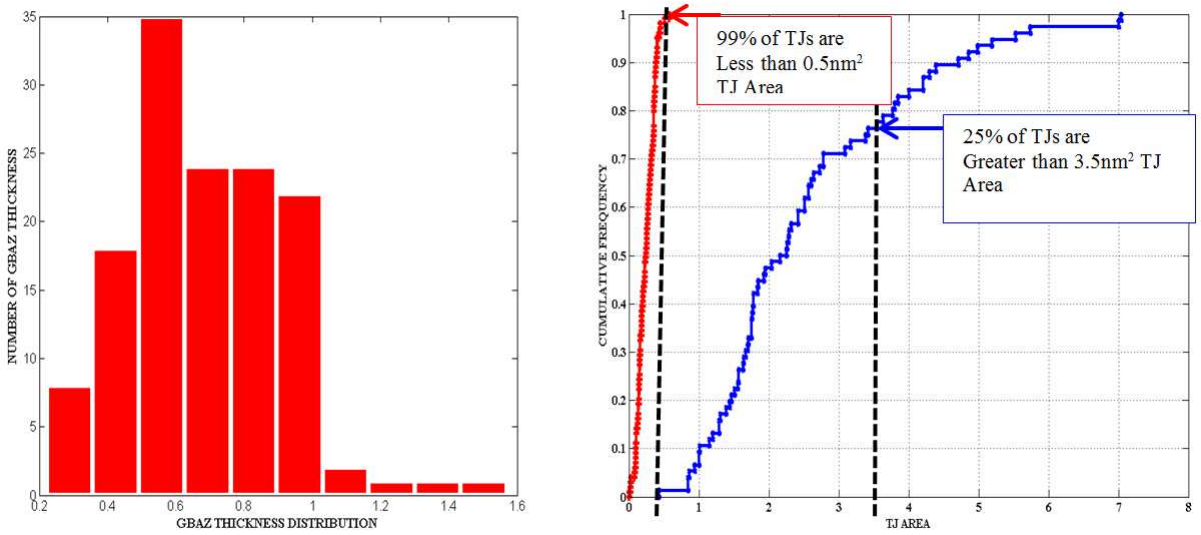

Fig. 15 (a) GBAZ thickness distribution and (b) cumulative frequency of TJ area distribution of the mesoscale microstructural model with sharp corner TJ (red line and its total area is 25.92nm^2) and round corner TJ (blue line and its total area is 187.14nm^2) models of NPC material.

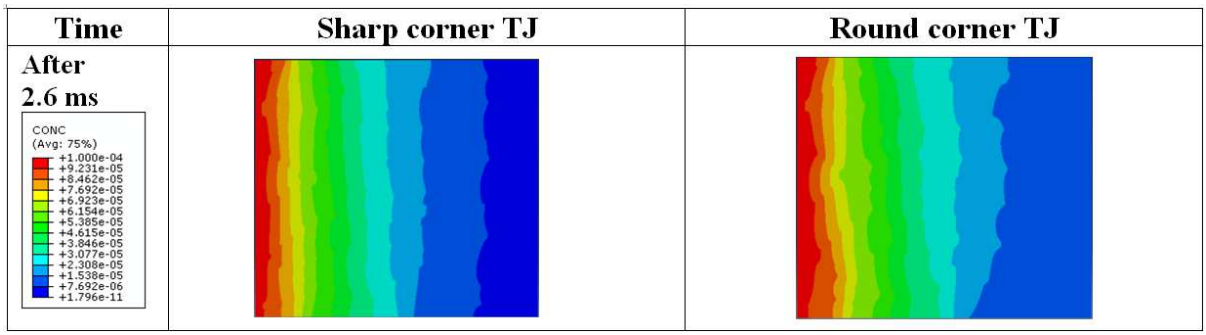

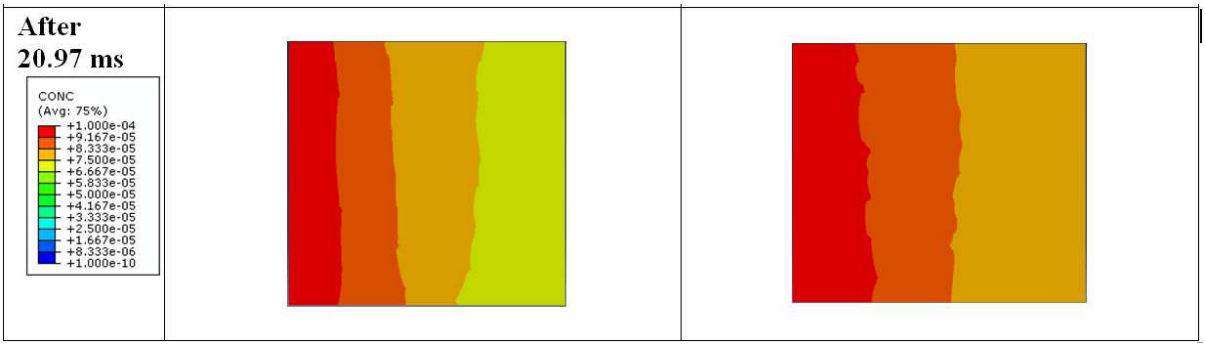

Fig. 16 The effect of TJ shape on hydrogen transport in the mesoscale microstructure of NPC material.

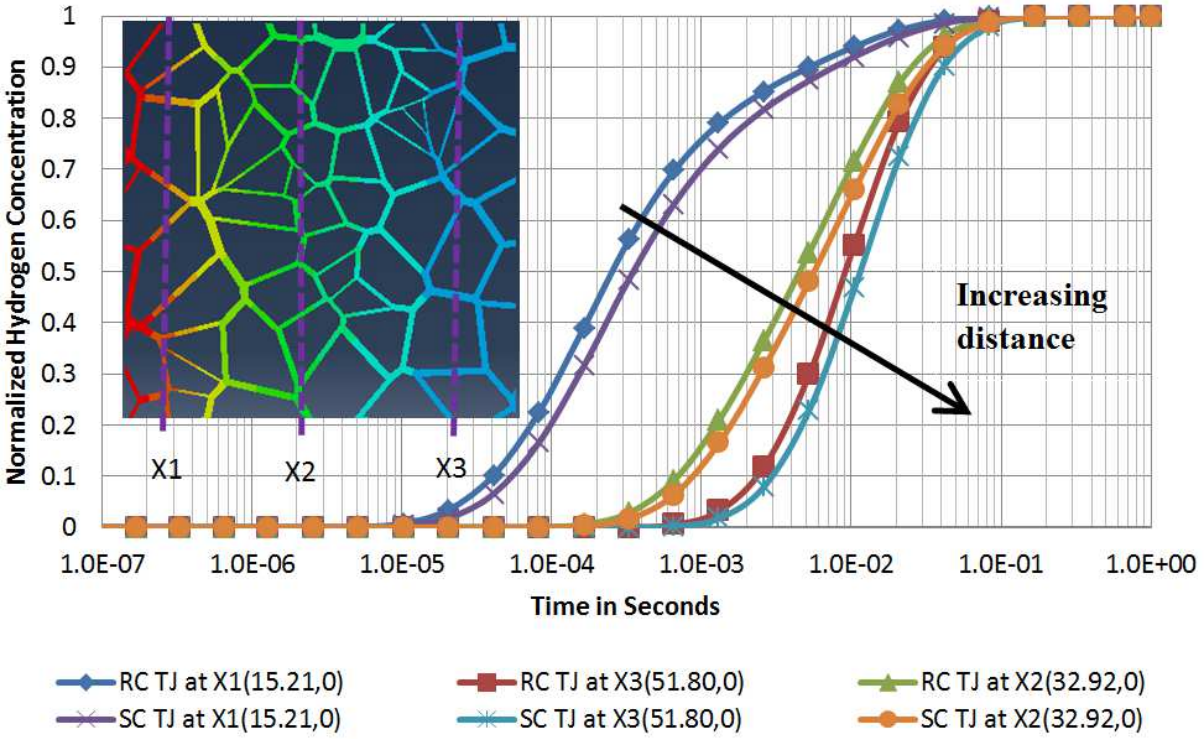

Fig. 17 The effect of sharp corner (SC) TJ and Round corner (RC) TJ on hydrogen concentration of NPC material for three different TJ at distances X1, X2 and X3 after the same elapsed time of one second.

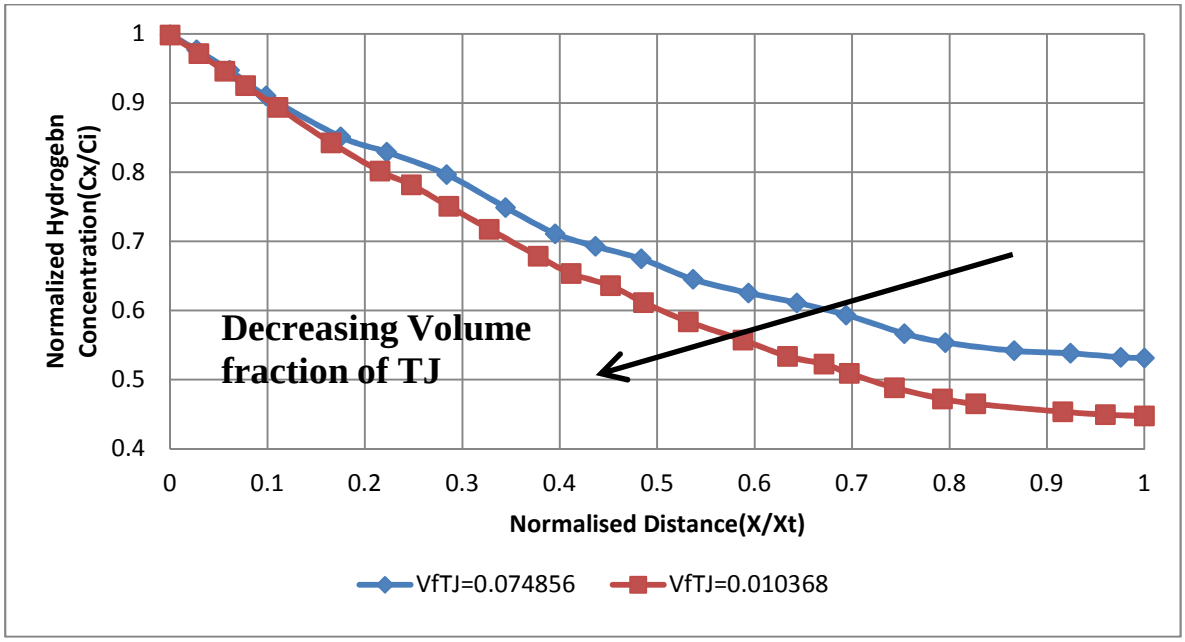

Fig. 18 Computed normalized hydrogen concentration dependency on normalized distance of NPC material with the same average grain size microstructures but two different volume fractions of TJ after 10 ms.

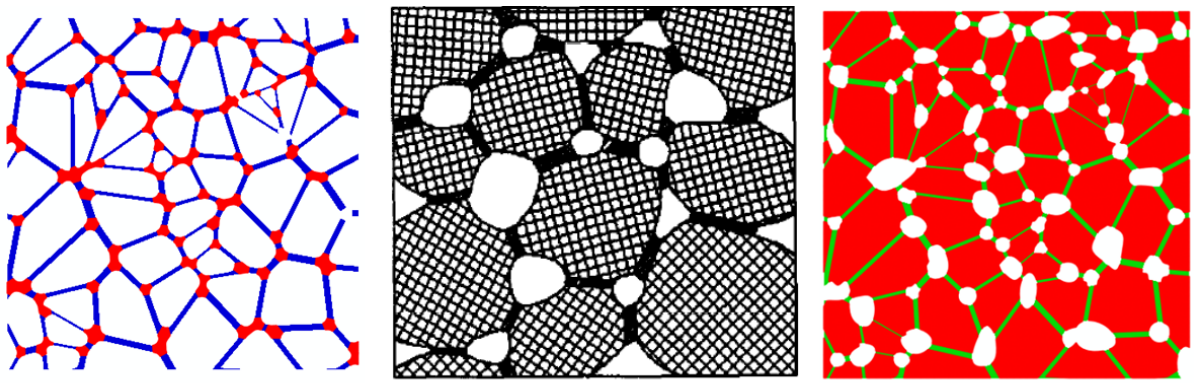

(a) (b) (c)

Fig. 19 (a) Fine grains in TJ (red) (b) a schematic of nanocrystalline material showing cluster boundaries involving pores in TJs(Bokstein et al. [5] and references therein) and (c) computationally generated nanocrystalline material similar to the schematic shown in (b).

Grain size /Time	1.3miliseeconds	83 milliseconds	167miliseconds
10nm with fine grain in TJ	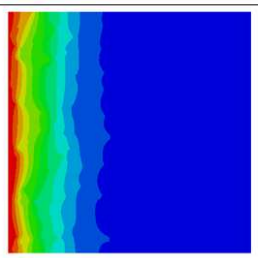	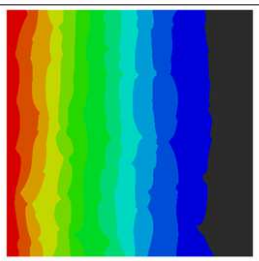	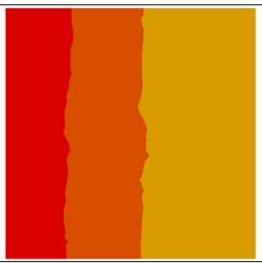

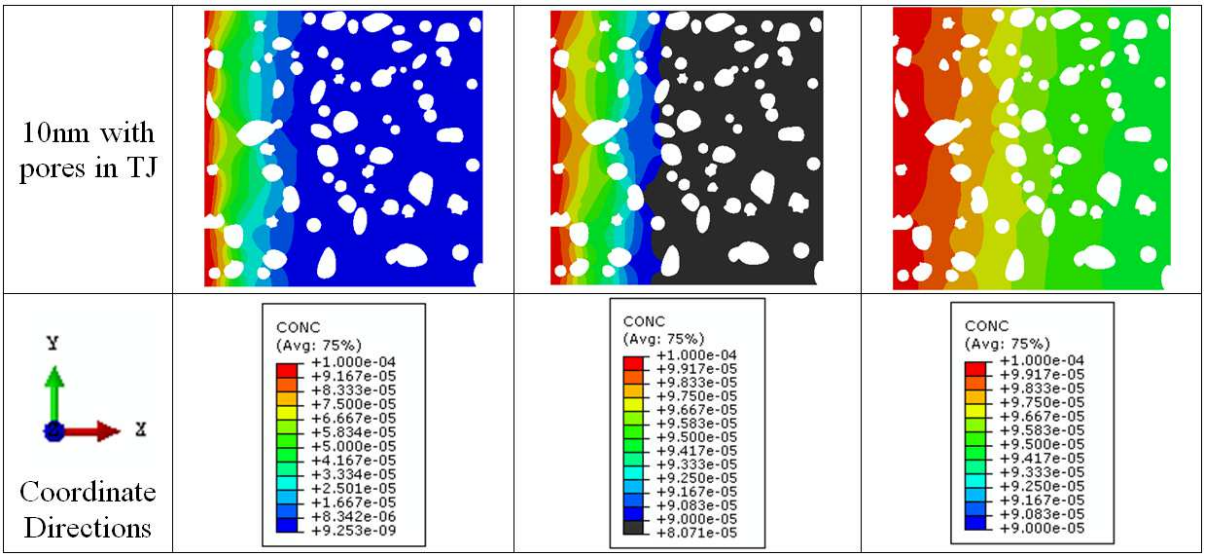

Fig. 20 (a) Hydrogen transport results from the computational analysis of two different synthetic microstructures with average grain size 10nm (a) with fine grain in TJs and (b) pores in TJs after three different time intervals.

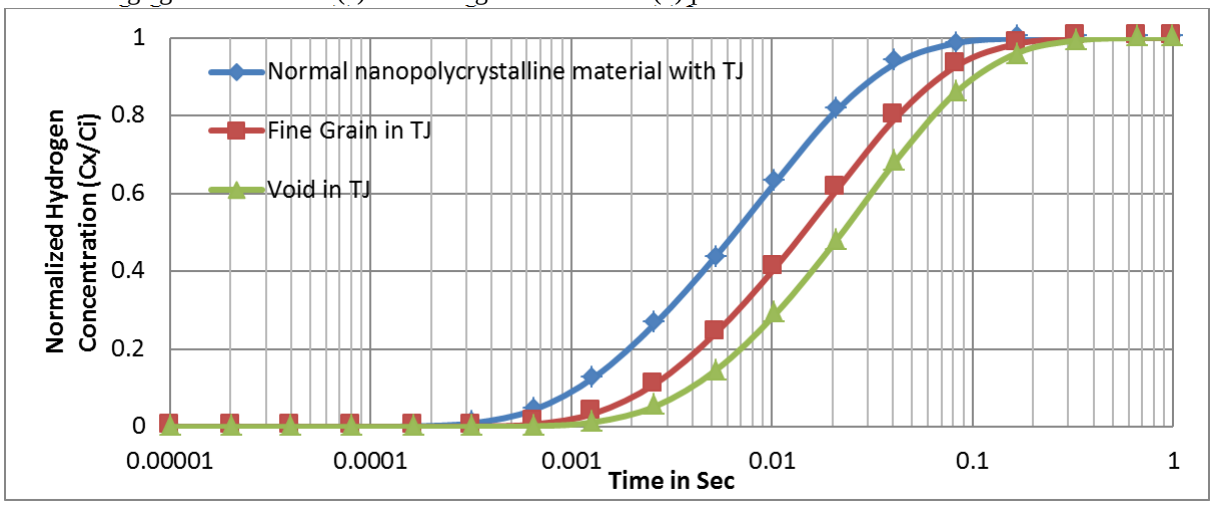

Fig. 21 Computed normalized hydrogen concentration dependency on time for 10nm grain size NPC materials with three different microstructures i.e. material with a microstructure containing TJs (blue line), fine nano grains in TJs (red line) and pores in TJs (green line).

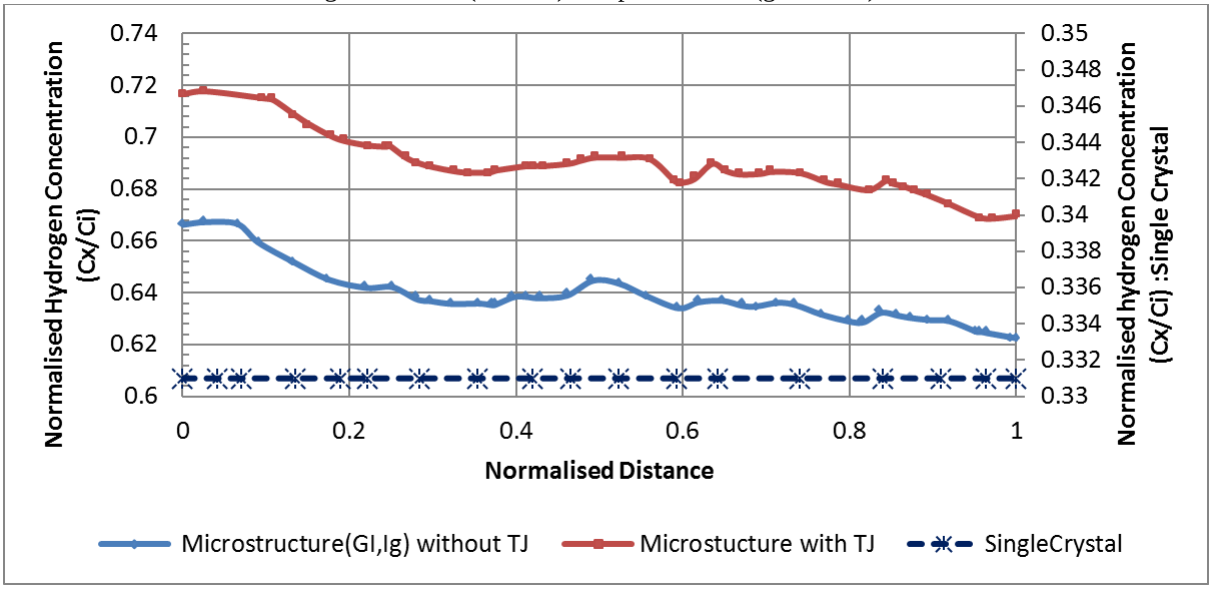

Fig. 22 Computed normalized hydrogen concentration dependency on normalized (Y/Yt) distance at a distance

(X/Xt) =0.65 for 10nm grain size NPC with a two phase microstructure (i.e. GI and Ig) without TJs, a three phase microstructure with TJs and single crystal nickel. The results were obtained at time = 10 ms.

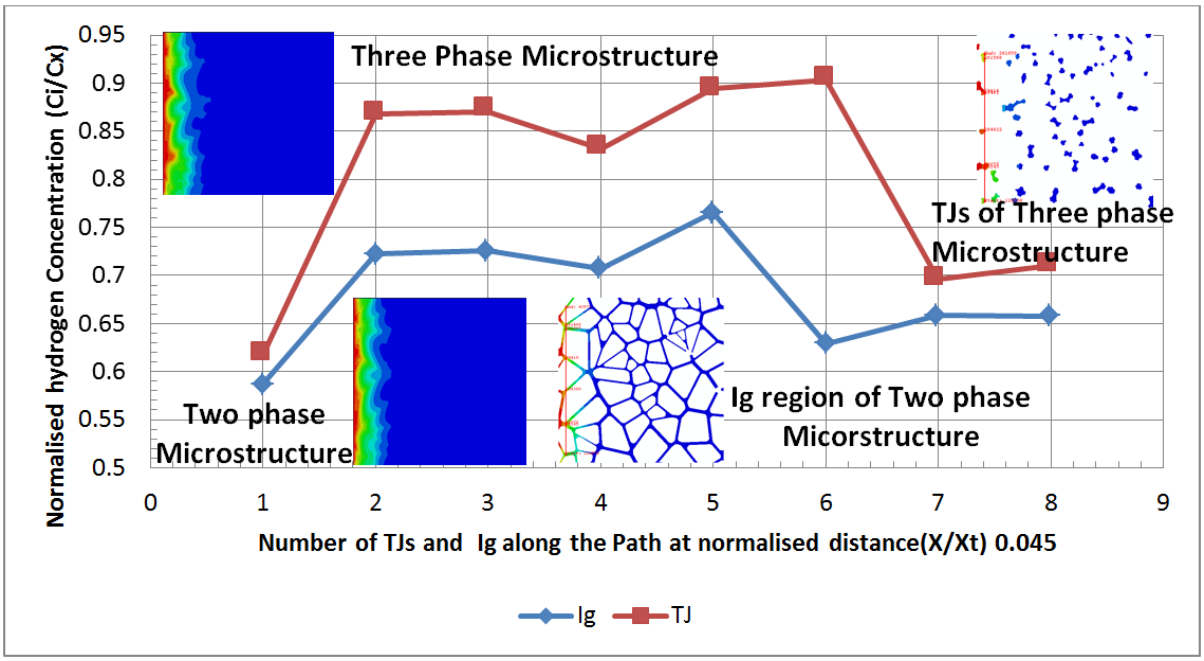

Fig. 23 Computed accumulated normalized hydrogen concentration dependency on i) number of TJs in three phase microstructural NPC nickel and ii) number of Ig in two phase microstructural NPC nickel along a path at a normalised distance (X/Xt)=0.045 at time 0.164ms.